POLITECNICO DI TORINO
Repository ISTITUZIONALE

UAV photogrammetry for archaeological site survey. 3D models at the Hierapolis in Phrygia (Turkey)

Original
UAV photogrammetry for archaeological site survey. 3D models at the Hierapolis in Phrygia (Turkey) / Chiabrando, F., D'Andria, F., Sammartano, G., Spanò, A.. - In: VIRTUAL ARCHAEOLOGY REVIEW. - ISSN 1989-9947. - ELETTRONICO. - 9:18(2018), pp. 28-43. [10.4995/var.2018.5958]

Availability:
This version is available at: 11583/2697610 since: 2018-01-17T11:21:24Z

Publisher:
Universitat Politècnica de València-Spanish Society of Virtual Archaeology

Published
DOI:10.4995/var.2018.5958

Terms of use:

This article is made available under terms and conditions as specified in the corresponding bibliographic description in the repository

Publisher copyright

(Article begins on next page)

27 November 2026

Smart Materials and Structures

PURPOSE-LED PUBLISHING™

PAPER • OPEN ACCESS

Shape sensing of viscoelastic structures using the inverse finite element method: numerical and experimental validation

To cite this article: Rinto Roy *et al* 2026 *Smart Mater. Struct.* **35** 115048

View the article online for updates and enhancements.

SmarAct | group

webinar

Watch on demand

One sample, many dimensions: prospects for multimodal nanoscale characterization

Explore how precise sample manipulation enables complementary nanoscale techniques to work together on one sample

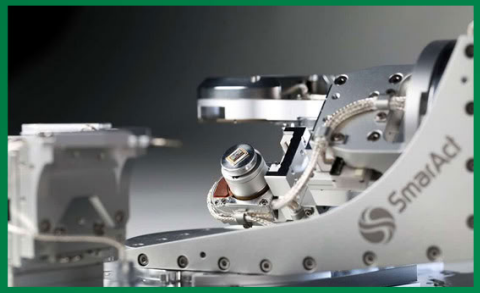

Now available to watch on demand

This content was downloaded from IP address 130.192.24.124 on 25/11/2026 at 12:22

Smart Materials and Structures

Check for updates

OPEN ACCESS

RECEIVED
11 April 2026

REVISED
12 October 2026

ACCEPTED FOR PUBLICATION
5 November 2026

PUBLISHED
25 November 2026

Original content from this work may be used under the terms of the Creative Commons Attribution 4.0 licence.

Any further distribution of this work must maintain attribution to the author(s) and the title of the work, journal citation and DOI.

PAPER

Shape sensing of viscoelastic structures using the inverse finite element method: numerical and experimental validation

Rinto Roy[1], **Marco Esposito**[1], **Vito Burgio**[2], **Marco Gherlone**[1] and **Cecilia Surace**[2,*]

[1] Department of Mechanical and Aerospace Engineering, Politecnico di Torino, Torino, Italy
[2] Bio Materials and Structures Laboratory, Department of Structural, Geotechnical and Building Engineering, Politecnico di Torino, Torino, Italy
[*] Author to whom any correspondence should be addressed.

E-mail: cecilia.surace@polito.it

Keywords: shape sensing, inverse finite element method (iFEM), viscoelastic structures, time-dependent behaviour, structural health monitoring, additive manufacturing

Abstract

The inverse Finite Element Method (iFEM) is well established for shape sensing of elastic structures, but its performance under time-dependent viscoelastic deformation remains insufficiently assessed. This work presents, to the authors" knowledge, the first combined numerical and experimental assessment of iFEM under creep and recovery conditions within the small-deformation regime. The objective is to determine whether time-dependent displacement fields can be reconstructed directly from strain histories without introducing a viscoelastic constitutive law, material parameters, load histories, or internal variables into the inverse analysis. Two complementary case studies are considered. First, a viscoelastic abdominal-patch model is analysed under sustained pressure, with a calibrated Generalised Maxwell model used only in the forward finite element simulation to generate reference strain and displacement fields. Second, an SLA-manufactured NACA 0016 airfoil beam is experimentally tested under loading and unloading, using measured strain histories as iFEM input and LVDT measurements for validation. In the numerical case, the maximum error in central transverse displacement is 2.46%, while the field-based normalised RMSE remains below 2.26%. In the experimental case, the reconstructed tip displacement differs from the LVDT measurements by less than 5% for most of the test, with larger discrepancies during unloading. The results show that the kinematics-based iFEM formulation can reconstruct creep and recovery histories directly from measured strains, while the material time dependence is conveyed through the strain data rather than through a constitutive model within the inverse analysis.

1. Introduction

Shape sensing, the reconstruction of full-field structural deformation from sparse measurements, has become an essential capability in modern engineering systems [1]. Its relevance spans aerospace [2], civil structures [3], biomechanics [4], and soft robotics [5], where real-time monitoring of flexible or compliant structures is required for safety [6], diagnostics [7], or closed-loop control [8]. Traditional approaches rely on dense sensor networks or full-field measurement techniques, which are often impractical, costly, or invasive. Other strategies, such as the integration of measured strains within classical theories [9] or the representation of displacement fields via prescribed basis functions [10], offer viable alternatives but are constrained by geometric assumptions, sensitivity to sensor density, or the need for system identification and extensive calibration. Purely data-driven approaches, including neural networks, have also been explored, yet they typically require large datasets and significant training effort [11].

Within this context, the inverse finite element method (iFEM) has emerged as a powerful and versatile alternative [12]. Built upon a least-squares variational principle and relying solely on strain—displacement relations, iFEM operates without the need to know details on the material properties or the

© 2026 The Author(s). Published by IOP Publishing Ltd

applied loads, for both static and dynamic applications. Its finite element framework naturally accommodates complex geometries and boundary conditions, while its capacity to reconstruct accurate deformation fields from sparse measurement sets has established it as a leading technique for shape sensing [12]. During the past two decades, significant contributions have applied the iFEM to plates and shells [13], to beams [14–16], to hybrid shell-beam structures [17] to composite laminates [18], sandwich configurations [19] and nonlinear materials [20]. These developments have been complemented by research on strain pre-extrapolation strategies [21, 22], optimal sensor placement [23, 24], numerical regularisation [25], applications such as damage detection of beam- and plate-like structures [26–29] and the monitoring of morphing wings [30].

Parallel to these methodological advances, additive manufacturing, commonly known as 3D printing, has become a key enabling technology in modern engineering [31]. Its ability to produce geometrically complex components with high precision and minimal material waste has expanded design possibilities across multiple fields. Among additive manufacturing techniques, stereolithography and other photopolymer-based methods are particularly attractive for producing high-resolution components from advanced resin systems [32]. These capabilities have opened new opportunities for lightweight structures, integrated functionalities, and customised mechanical performance [33, 34].

A particularly promising class of 3D-printed materials is viscoelastic photopolymer resins, which exhibit a combination of instantaneous elastic and time-dependent viscous responses [35]. Such materials are increasingly employed in applications where damping, energy dissipation, or long-term deformation behaviour are critical—ranging from civil and automotive components to aerospace structures and biomechanical devices [36]. In addition to additively manufactured resins, a broad range of biopolymers and soft polymeric materials used in biomedical devices, such as wound dressings, transdermal patches, and other tissue-contacting components, are inherently viscoelastic even when they are not fabricated via 3D printing. These materials play an important role in facilitating wound healing and tissue regeneration [37] while exhibiting time-dependent mechanical behaviour relevant to device performance and comfort.

However, their inherently time-dependent behaviour, coupled with potential anisotropies or defects introduced during layer-by-layer fabrication, poses significant challenges for accurate modelling and monitoring. As a result, the extension of shape-sensing techniques such as iFEM to viscoelastic structures is of growing importance. While traditional finite element models require accurate characterisation of time-dependent constitutive behaviour, inverse methods offer the potential to reconstruct deformation histories directly from sparse measurement data.

Previous studies have addressed shape monitoring and reconstruction in polymeric, soft, and highly compliant structures using different sensing and reconstruction strategies. Li *et al* employed embedded fibre Bragg grating sensors to monitor the deformation and recovery of shape-memory polymer structures during deployment [38], with the main objective of tracking thermally activated shape recovery. Lun *et al* focused instead on real-time surface-shape reconstruction of soft elastomeric structures from sparse local strain measurements, combining embedded FBG sensing with numerical and data-driven reconstruction [39]. More recently, Feliu-Talegon *et al* investigated shape and configuration estimation of soft robotic structures using embedded multidimensional strain sensors coupled with strain-based kinematic modelling [40]. Although these studies are relevant because they address shape reconstruction in highly compliant polymeric structures, their objectives differ from that of the present work: they primarily address shape-memory recovery, real-time shape estimation, or shape reconstruction of soft robotic systems, rather than the reconstruction of structural creep and recovery caused by viscoelastic material behaviour.

Despite the relevance of viscoelasticity in emerging engineering applications, the use of iFEM for time-dependent materials remains comparatively underexplored. Viscoelastic phenomena such as creep, stress relaxation, and rate-dependent stiffness produce time-dependent strain fields that are not explicitly modelled within the iFEM formulation. Addressing these challenges is essential for enabling realistic, deployable sensing and monitoring solutions across multiple domains.

This work contributes to this emerging research direction by presenting two complementary case studies designed to evaluate the performance of iFEM in reconstructing deformation under creep and recovery. The first involves a numerical model of a viscoelastic plate inspired by a biomedical abdominal patch subjected to physiological pressure. The second focuses on an experimental airfoil-shaped beam additively manufactured via stereolithography and exhibiting time-dependent deformation. Together, these case studies provide a combined numerical–experimental assessment of iFEM applied to time-dependent deformation, demonstrating its feasibility, limitations, and potential across different structural engineering contexts. The present assessment specifically focuses on creep under sustained loading and on the delayed recovery observed after unloading in the experimental case. Accordingly, the central question addressed in this study is whether the kinematics-based iFEM formulation adopted here can

reconstruct creep and recovery histories directly from strain measurements without introducing a viscoelastic constitutive law, material parameters, load histories, or additional internal variables into the inverse analysis.

2. Methods: inverse finite element formulation

In this section, the iFEM is briefly described.

The method is based on the discretisation of the structural domain using finite elements, which may be one-dimensional [41] or two-dimensional [13]. This discretisation leads to the definition of the displacement field in terms of shape functions and nodal degrees of freedom [42].

By differentiating the shape functions with respect to the spatial coordinates, one obtains the discretised strain field expressed in terms of the nodal DOFs:

$$\mathbf{e}\left(\mathbf{u}^{e}\right)=\mathbf{B}\mathbf{u}^{e}, \tag{1}$$

where vector $\mathbf{e}$ collects the strain measures associated with the element, and $\mathbf{B}$ denotes the matrix containing the derivatives of the shape functions. The explicit form of $\mathbf{B}$, the nodal vector $\mathbf{u}^{e}$, and the strain components in $\mathbf{e}(\mathbf{u}^{e})$ depend on the specific inverse element formulation adopted.

The strain field representation in equation (1) can be used to determine the nodal DOFs that best reproduce a measured strain field at discrete locations. For each element in the mesh, the squared error between the measured strain field $\mathbf{e}^{m}$ and the analytical one computed via equation (1) is defined. For beam elements based on Timoshenko beam theory [41], the associated error functional reads:

$$\Phi_{e}\left(\mathbf{u}^{e}\right)=\sum_{k=1}^{6}\lambda_{b_k}w_{b_k}\sum_{i=1}^{N}\frac{1}{\ell_{e}}\left[e_{k}\left(x_{i}\right)-\left(e_{k}^{m}\right)_{i}\right]^{2}, \tag{2}$$

where $e_k(x_i)$ is the kth analytical sectional strain evaluated at the axial position x_i, $\left(e_k^m\right)_i$ is the corresponding measured sectional strain from a sensor, N is the number of Sections along the element where strains are recorded, and ℓ_e denotes the element length. The index k spans the six sectional strains of the Timoshenko beam theory: axial strain ($k=1$), bending curvatures ($k=2,3$), transverse shear strains ($k=4,5$), and torsional strain ($k=6$). For very slender beams, an iFEM formulation based on the Bernoulli-Euler beam theory is also available [43] where equation (2) holds with the first sum ranging over $k=1:3$, thus including only axial and bending strain measures. The scaling coefficients λ_{b_k} ensure dimensional consistency, whereas the weights w_{b_k} account for missing strain information, taking the value 1 when the corresponding strain measure is measured and a small number (10^{-5}) otherwise.

For shell elements, a similar error functional may be formulated as:

$$\Phi_{e}\left(\mathbf{u}^{e}\right)=\sum_{k=1}^{8}\lambda_{p_k}w_{p_k}\iint_{A_e}\left[e_{k}\left(\mathbf{u}^{e}\right)-e_{k}^{m}\right]^{2}\mathrm{d}x\mathrm{d}y, \tag{3}$$

where $e_k(\mathbf{u}^e)$ is the analytical strain measure, e_k^m the corresponding measured value, and A_e the area of the shell element. For a Mindlin plate, the eight strain measures include: membrane strains ($k=1,2,3$), bending and torsion curvatures ($k=4,5,6$), and transverse shear strains ($k=7,8$). The coefficients λ_{p_k} and w_{p_k} play the same role as in the beam formulation; however, since transverse shear strains cannot be directly recorded by typical strain sensors, the weights w_{p_7} and w_{p_8} are always fixed at 10^{-5}.

Minimising the error functional with respect to the nodal DOFs yields a system of linear equations. For beam elements one obtains:

$$\frac{\partial\Phi_{e}}{\partial\mathbf{u}^{e}}=\mathbf{k}_{e}^{b}\mathbf{u}^{e}-\mathbf{f}_{e}^{b}=\mathbf{0}, \tag{4}$$

and for shell elements:

$$\frac{\partial\Phi_{e}}{\partial\mathbf{u}^{e}}=\mathbf{k}_{e}^{p}\mathbf{u}^{e}-\mathbf{f}_{e}^{p}=\mathbf{0}, \tag{5}$$

where $\mathbf{k}_e^b$ and $\mathbf{k}_e^p$ denote the element stiffness-like matrices arising from the minimisation, and $\mathbf{f}_e^b$, $\mathbf{f}_e^p$ are the element load-like vectors.

Applying the standard finite element assembly procedure over the whole mesh, and introducing the required transformations from local to global DOFs, leads to a global system of linear equations. After

enforcing boundary conditions, the global displacement vector $\mathbf{U}$ that best fits the measured strains in the least-squares sense is obtained from:

$$\mathbf{U} = \mathbf{K}^{-1}\mathbf{F}, \tag{6}$$

where the matrix $\mathbf{K}$ depends solely on the mesh and the sensor configuration, whereas the vector $\mathbf{F}$ depends additionally on the current measured strains. A crucial aspect is that, once the sensor layout is fixed, $\mathbf{K}$ remains constant over time. Hence its inversion needs to be performed only once. At each measurement instant, only the vector $\mathbf{F}$ changes, and the displacement reconstruction relies on simple matrix–vector multiplication, which renders real-time structural monitoring feasible. In other words, in time-dependent applications, the measured strain field can be explicitly expressed as a function of time, i.e. $\mathbf{e}^m = \mathbf{e}^m(t)$. Accordingly, the iFEM formulation can be interpreted as a sequence of instantaneous inverse problems, where at each time instant t the displacement field is reconstructed from the corresponding strain measurements. From a variational standpoint, this corresponds to the minimisation of a time-indexed least-squares functional:

$$\mathbf{U}(t) = \arg\min_{\mathbf{U}} \Phi(\mathbf{U}; t), \tag{7}$$

Here, arg min denotes the argument that minimises the functional, i.e. the displacement field that best fits the measured strain data in a least-squares sense. The time dependence is entirely embedded in the measured strain field, while the kinematic relations governing the inverse formulation remain unchanged. In the typical case where the sensor configuration remains unchanged over time, the system of equations (6) simply changes as follows

$$\mathbf{U}(t) = \mathbf{K}^{-1}\mathbf{F}(t), \tag{8}$$

practically implying the solution of a linear system at any time by updating the global force-like vector $\mathbf{F}(t)$ according to the variation of strains. Equation (8) is solved independently at each measurement instant. No temporal regularisation or continuity constraint is imposed between successive time steps, and no internal variables describing the material history are introduced. Therefore, the displacement field reconstructed at $(t+\Delta t)$ depends only on the strain measurements available at that instant and not on the displacement field reconstructed at (t). The formulation should thus be interpreted as a sequence of instantaneous kinematic inverse problems. Although the physical response of a viscoelastic structure is history-dependent, the consequences of this material history are already contained in the strain measurements supplied to iFEM. The method transfers this time-dependent strain information to the reconstructed displacement field; it does not predict the subsequent viscoelastic evolution or identify its constitutive parameters.

3. Results and discussion

3.1. Overview

Viscoelastic materials exhibit a combined elastic and viscous response, resulting in deformation behaviour that depends not only on the magnitude of the applied loads but also on their duration and loading history. Under sustained stress, such materials may undergo creep, while under imposed strain they may experience stress relaxation. In addition, their stiffness is generally rate-dependent, reflecting the intrinsic time-dependent nature of the material response. These characteristics are particularly relevant for polymeric and biopolymeric materials, which are increasingly adopted in lightweight structures, additive manufacturing, and biomedical applications.

From a structural modelling and monitoring perspective, viscoelasticity introduces significant challenges. The mechanical response of viscoelastic structures cannot be fully described by instantaneous stress–strain relationships, but requires constitutive models incorporating internal variables and time-evolution laws. Such models must be carefully calibrated and validated, as uncertainties in material parameters may significantly affect predictive accuracy. Consequently, the reliable identification of structural deformations in viscoelastic systems demands approaches capable of handling time-dependent behaviour while remaining robust with respect to constitutive modelling assumptions.

In this context, iFEM reconstructs displacement fields by enforcing kinematic compatibility through strain-displacement relations, without explicitly requiring material properties or applied loads. In a time-dependent application, the strain measurements available at each instant are mapped into the corresponding displacement field. Consequently, the effects of creep or recovery already present in the measured strain histories are reflected in the reconstructed deformation. However, iFEM does not model or

predict the evolution of these phenomena and does not replace a constitutive viscoelastic model when prediction of the future structural response is required.

In the numerical case study, a viscoelastic plate inspired by a biomedical abdominal patch is analysed using a forward finite element model incorporating a viscoelastic Generalised Maxwell model calibrated against experimental stress-relaxation data. This constitutive model is used exclusively to generate time-dependent reference strain and displacement fields under sustained physiological loading. It is not part of the iFEM formulation, and none of its constitutive parameters is supplied to the inverse reconstruction. Conversely, in the experimental case study involving an additively manufactured airfoil-shaped beam, the time-dependent response of the structure is inherently embedded in the measured strain histories used as input to the inverse analysis. This dual approach enables a comprehensive assessment of the capabilities and limitations of iFEM, both in a controlled numerical environment and in a realistic experimental scenario characterised by viscoelastic behaviour.

3.2. Numerical case study: viscoelastic abdominal patch

3.2.1. Geometry and problem definition

The numerical case study considers a thin viscoelastic plate representing an abdominal patch designed to provide temporary mechanical support to the abdominal wall during the healing process following hernia repair.

Abdominal hernias are commonly treated using sutures and surgical meshes; however, these approaches may lead to complications such as tissue ischemia and recurrence due to local stress concentrations and elevated intra-abdominal pressure. In this context, the development of a compliant and biodegradable reinforcing patch represents a promising strategy to improve load distribution and reduce re-injury risk.

The patch is modelled as a square plate with dimensions 100×100 mm and a uniform thickness of 0.5 mm. It is subjected to a distributed transverse pressure representing intra-abdominal loading conditions, while its fixation to the surrounding tissue is idealised through discrete constraint points corresponding to sutures or tacks.

This simplified representation captures the essential mechanical behaviour of sutured patches, where deformation is governed by the interaction between localised fixation and distributed loading. In particular, the discrete supports allow the patch to deform between fixation points, generating smooth displacement fields representative of real implant behaviour.

The aim of this model is not to reproduce a fully detailed physiological environment, but to provide a controlled and mechanically meaningful benchmark for evaluating the performance of the iFEM in reconstructing time-dependent deformation fields in viscoelastic structures.

3.2.2. Material characterisation

The material adopted for the present numerical study originates from a prior experimental characterisation campaign conducted at the *Bio Materials and Structures Laboratory (BIOMAST Lab)*—Department of Structural, Building and Geotechnical Engineering, Politecnico di Torino (biomast.polito.it).

The experimental activity was aimed at investigating the mechanical behaviour of a biodegradable and biocompatible polymeric blend developed for biomedical applications, including implantable devices and soft tissue reinforcement systems.

Within this context, the characterised material was selected as a representative viscoelastic polymer for the present study. This choice allows grounding the numerical model on experimentally measured properties, ensuring a realistic description of the time-dependent behaviour while maintaining consistency with potential biomedical applications.

Accordingly, this section briefly summarises the experimental procedures adopted for material characterisation and presents the constitutive model selected for implementation in the finite element simulations.

The material consists of a polymeric blend of two commercially available biodegradable biopolymers in a 50:50 weight ratio: Resomer® LR 704 S (Poly L-lactide-co-D,L-lactide, P(L/DL)LA) and Resomer® LC 703 S (Poly L-lactide-co-ε-caprolactone, PLCL), both supplied by Evonik [44]. This combination enables tailoring of the mechanical response by combining the relatively high stiffness of lactide-based polymers with the enhanced ductility and viscoelastic behaviour of caprolactone-based polymers [45].

The biopolymeric blend was prepared by melt extrusion using a twin-screw extruder, followed by injection moulding to produce dog-bone specimens with the Type 5A geometry specified in ISO 527-2. Details on the manufacturing process are reported in [46].

The experimental campaign included uniaxial tensile tests and stress relaxation tests in order to characterise both the instantaneous elastic response and the time-dependent behaviour of the material. All

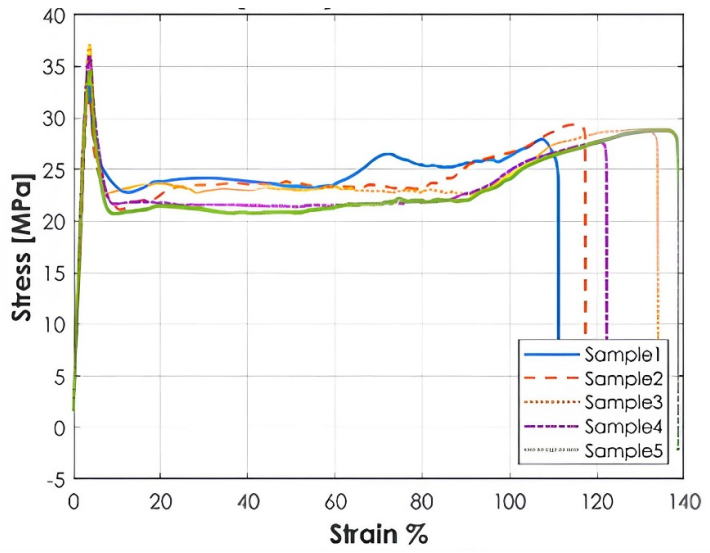

Figure 1. Stress–strain curves obtained from uniaxial tensile tests on P(L/DL)LA/PLCL specimens.

Table 1. Mechanical parameters obtained from the uniaxial tensile tests on P(L/DL)LA/PLCL specimens. Mean values and standard deviations are also reported.

	E_0 [MPa]	σ_Y [MPa]	ε_Y [%]	σ_B [MPa]	ε_B [%]
Sample 1	902.04	33.08	3.20	27.72	108.16
Sample 2	990.97	32.36	3.41	28.42	117.33
Sample 3	1093.97	37.12	3.62	28.13	133.54
Sample 4	967.68	36.02	3.62	27.07	122.03
Sample 5	771.15	34.43	3.63	28.05	138.24
Mean $\bar{X}$	945.16	34.60	3.49	27.88	123.86
Std. Dev.	119.25	1.98	0.20	0.51	12.17

tests were performed using an MTS Insight® electromechanical testing system equipped with a 1000 N load cell under displacement-controlled conditions.

Uniaxial tensile tests were conducted at a constant crosshead speed of 5 mm/min, consistent with testing conditions reported in the literature for PLA/PCL-based biodegradable polymer blends [47, 48], with a sampling frequency of 50 Hz. The resulting stress–strain curves, shown in figure 1, were used to evaluate the initial elastic properties of the material, yielding an average Young's modulus of $E_0 = 945$ MPa (see table 1).

The measured Young's modulus exhibited a standard deviation of 119.25 MPa, corresponding to a coefficient of variation of approximately 12.6%. This specimen-to-specimen variability may be associated with small local differences introduced during melt blending and injection moulding, including variations in phase distribution, morphology and thermal history. Accordingly, the measured mean modulus is used in the present study as a representative value for the forward numerical benchmark under the adopted testing conditions.

Stress-relaxation tests were performed at prescribed strain levels of 3%, 6%, and 8%, with a holding time of 300 s and a sampling frequency of 50 Hz. These levels were selected to characterise the strain-dependent relaxation response of the material over the investigated deformation range.

The measured stress evolution over time, reported in figure 2, exhibits a clear viscoelastic behaviour characterised by an initial elastic response followed by a gradual stress decay during the holding phase.

A Poisson's ratio of $\nu = 0.5$ was assumed, consistent with typical values for semicrystalline polymeric materials.

To model the time-dependent behaviour of the material, a Generalised Maxwell model was adopted. The shear relaxation modulus is expressed as:

$$G(t) = G_\infty + \sum_{i=1}^{N} G_i \exp\left(-\frac{t}{\tau_i}\right) \tag{9}$$

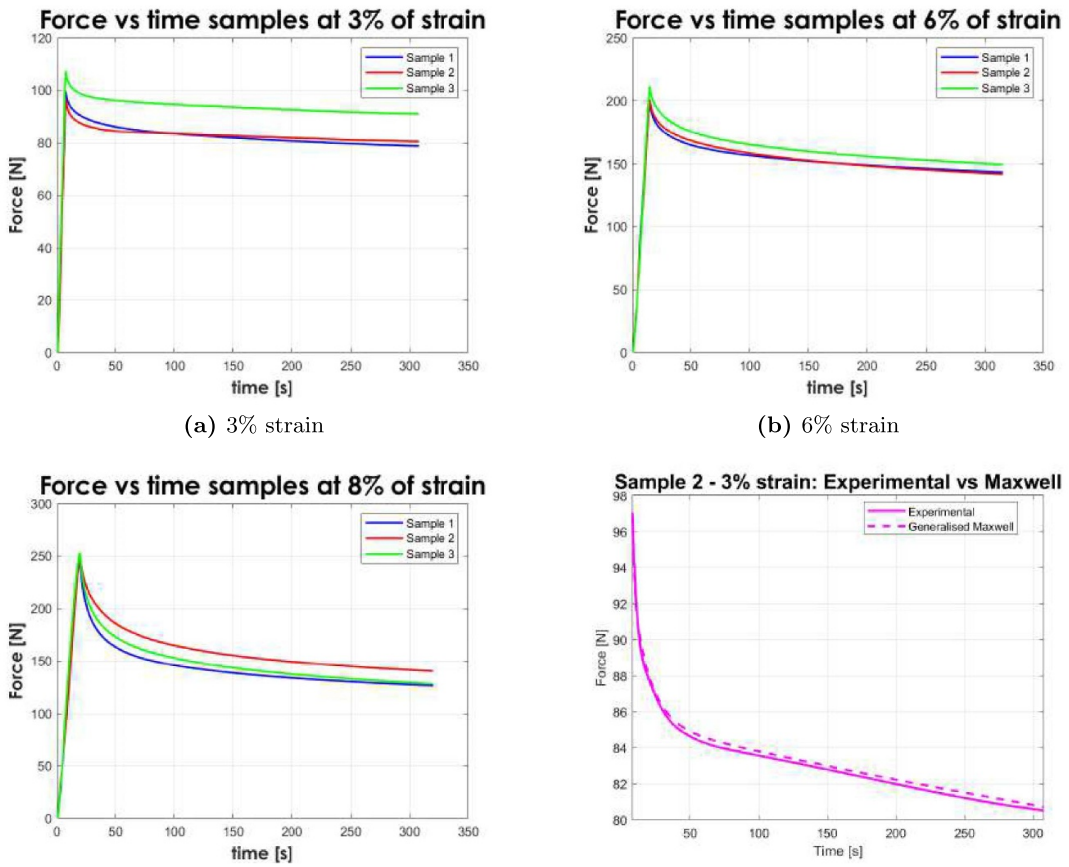

(a) 3% strain (b) 6% strain

(c) 8% strain (d) Specimen 2 at 3% strain

Figure 2. Stress-relaxation response of the P(L/DL)LA/PLCL blend at prescribed strain levels of (a) 3%, (b) 6%, and (c) 8%. (d) Comparison between the experimental relaxation response of Specimen 2 at 3% strain and the response reconstructed using the corresponding three-branch Generalised Maxwell parameters.

where G_∞ represents the long-term equilibrium modulus, G_i are the moduli associated with the Maxwell branches, and τ_i are the corresponding relaxation times.

The model parameters were identified through nonlinear least-squares fitting of the experimental relaxation curves using a Levenberg–Marquardt algorithm. A three-term Prony series ($N = 3$) was found to accurately reproduce the experimental response across all strain levels, with coefficients of determination close to $R^2 \approx 0.99$.

The complete experimental characterisation and model-identification procedure is reported in Rodriguez Reinoso *et al* [49].

To provide direct evidence of the ability of the selected parameter set to reproduce the measured time-dependent response, the relaxation curve of Specimen 2 at 3% strain was reconstructed using the corresponding three-branch Generalised Maxwell parameters and compared with the experimental curve, as shown in figure 2(d). The model reproduces both the rapid initial decrease and the subsequent slower relaxation over the 300 s holding period. This agreement is consistent with the coefficient of determination ($R^2 = 0.99$) reported for this specimen.

For normalisation of the experimentally identified Generalised Maxwell parameters, the instantaneous shear modulus is calculated from the fitted moduli as

$$G_0 = G_\infty + \sum_{i=1}^{N} G_i, \tag{10}$$

where G_∞ and G_i are obtained from the nonlinear fitting of the experimental relaxation data. Thus, G_0 is not an independently fitted parameter, but is calculated from the identified Maxwell moduli. Equation (9) can then be equivalently rewritten as

$$G(t) = G_0 \left[\alpha_\infty^G + \sum_{i=1}^{N} \alpha_i^G \exp\left(-\frac{t}{\tau_i}\right) \right], \tag{11}$$

Table 2. Generalised Maxwell parameters identified for Specimen 2 at 3% strain. The absolute moduli refer to the original experimental relaxation fit, whereas the normalised coefficients and relaxation times define the relaxation parameters adopted in the ANSYS implementation.

Parameter	Absolute modulus [MPa]	Normalised coefficient	Relaxation time [s]
Equilibrium	$G_\infty = 95.16$	$\alpha_\infty^G = 0.71$	—
Branch 1	$G_1 = 10.22$	$\alpha_1^G = 0.08$	$\tau_1 = 12.66$
Branch 2	$G_2 = 5.90$	$\alpha_2^G = 0.04$	$\tau_2 = 1.49$
Branch 3	$G_3 = 22.88$	$\alpha_3^G = 0.17$	$\tau_3 = 903.23$

where the normalised coefficients are defined as

$$\alpha_i^G = \frac{G_i}{G_0}, \qquad \alpha_\infty^G = \frac{G_\infty}{G_0}. \tag{12}$$

The normalised coefficients describe the relative contribution of the equilibrium modulus and of each Maxwell branch to the time-dependent material response. The quantity G_0 is used here only to normalise the fitted Maxwell moduli and should not be interpreted as an additional parameter independently identified from the experimental data.

For the present numerical application, the parameter set identified for Specimen 2 at 3% strain was selected. The complete set of absolute Generalised Maxwell parameters and corresponding normalised Prony coefficients is summarised in table 2.

The equilibrium modulus G_∞ was obtained as a fitted parameter of the Generalised Maxwell model rather than directly from the final experimental data point. It represents the asymptotic modulus reached as $t \to \infty$.

For implementation in ANSYS Mechanical, the normalised Prony coefficients and corresponding relaxation times were introduced into the time-domain viscoelastic formulation, while the instantaneous material stiffness was specified independently through the Young's modulus E_0 and Poisson's ratio ν. These inputs jointly define a single small-strain viscoelastic constitutive response: the elastic properties establish the instantaneous stiffness, whereas the Prony terms govern its time-dependent relaxation.

Within the assumed linear-viscoelastic regime, the experimentally calibrated relaxation parameters were used in the forward ANSYS analysis to generate a representative time-dependent response under sustained pressure. In the present study, the Generalised Maxwell model is used solely to provide reference strain and displacement fields for the numerical benchmark; neither the constitutive model nor its parameters enters the subsequent iFEM reconstruction.

3.2.3. Finite element model

The numerical simulation of the abdominal patch was carried out using ANSYS Workbench 2023 R2. The patch geometry consists of a square plate with dimensions 100×100 mm and a uniform thickness of 0.5 mm.

The geometry was imported as a surface and subsequently discretised using Shell181 elements, which are suitable for modelling thin structures undergoing bending-dominated deformation. The shell thickness was assigned directly within the element formulation.

The mesh was generated using a structured discretisation, with ten elements along each edge of the plate, ensuring a sufficient spatial resolution to capture the deformation field while maintaining computational efficiency.

The material behaviour was defined based on the experimental characterisation described in section 3.2.2. The instantaneous material stiffness was specified through the Young's modulus $E_0 = 945$ MPa and Poisson's ratio $\nu = 0.5$, while its time-dependent relaxation was defined through the normalised Prony coefficients and corresponding relaxation times. These inputs jointly define a single small-strain viscoelastic constitutive model in ANSYS: the elastic constants establish the instantaneous stiffness, whereas the Prony series describes its time-dependent relaxation. Thus, the Prony series does not represent an additional constitutive response superimposed on an independent linear-elastic response.

The normalised Prony coefficients and relaxation times identified for Specimen 2 at 3% strain were adopted because this was the lowest investigated strain level and therefore the closest to the small-strain regime considered in the patch simulation.

The maximum loading condition was defined as a uniformly distributed pressure applied on the lower surface of the patch, representing intra-abdominal pressure. Based on literature data, a pressure

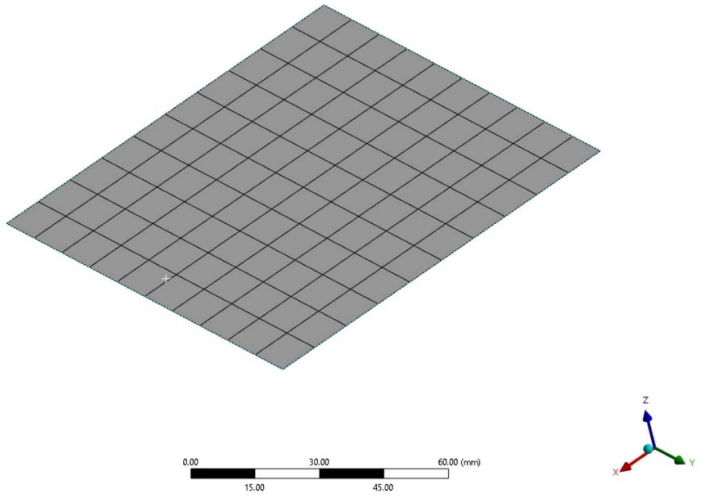

Figure 3. Finite element model of the abdominal patch showing the shell discretisation.

value of 0.0092 MPa was selected to simulate physiological conditions during dynamic activities such as jumping [50].

The boundary conditions were applied at discrete nodes along the patch edges to represent idealised attachment points associated with sutures or tacks. The (10×10) structured discretisation gives a distance of approximately 10 mm between consecutive boundary nodes. This spacing was deliberately selected so that each constrained boundary node could represent a potential attachment location. At these nodes, the translational degrees of freedom were constrained, whereas the out-of-plane rotational degrees of freedom remained free; the patch was therefore supported at discrete locations rather than continuously clamped.

Different numbers, spacings or non-uniform distributions of attachment points would primarily modify the local strain field and generate localised perturbations near the constrained nodes. Outside these boundary-disturbance regions, the global displacement field is expected to be comparatively less sensitive, particularly for the regular attachment spacing and smooth pressure loading considered here. Nevertheless, the adopted boundary conditions represent an idealised numerical benchmark rather than a detailed model of a specific clinical suture configuration. The reconstruction errors reported in this study are therefore conditional on this assumption, and a systematic sensitivity analysis would be required to quantify the influence of alternative suture patterns.

The time-dependent simulation was carried out in two loading stages, while the same viscoelastic constitutive model remained active throughout the entire analysis. During the first stage, the pressure was rapidly increased from 0 to 0.0092 MPa over 1 s, resulting in a response dominated by the instantaneous stiffness of the material. During the second stage, the pressure was maintained constant at 0.0092 MPa for 899 s, allowing the time-dependent creep response to develop. The two stages therefore represent different loading conditions of the same viscoelastic material rather than separate elastic and viscoelastic material responses. The two loading stages can be clearly observed by analysing the time history of an example strain measurement in figure 4. The plot highlights the viscoelastic response of the patch under constant loading. In particular, it shows a progressive increase in strain over time despite the load remaining constant, which is characteristic of viscoelastic behaviour.

Figure 5(a) shows the displacement field for the simulation at the last step of the analysis, where the maximum deformation is obtained. For each time step of the simulation, the strain data for the application of the iFEM and the displacement fields, used as a reference for the evaluation of the shape sensing, are extracted.

3.2.4. iFEM Reconstruction

The FE model used to simulate the patch and to perform the iFEM analysis, in terms of mesh and BCs, is the same as that adopted for the direct ANSYS analysis of the patch (figures 3 and 6). For this analysis, the formulation adopted for the inverse Quad elements is the one described in detail in [51].

In order to simulate a more realistic condition, instead of using the full set of strains available in this type of numerical application, a reduced set of strain sensors is considered. In selecting the sensor

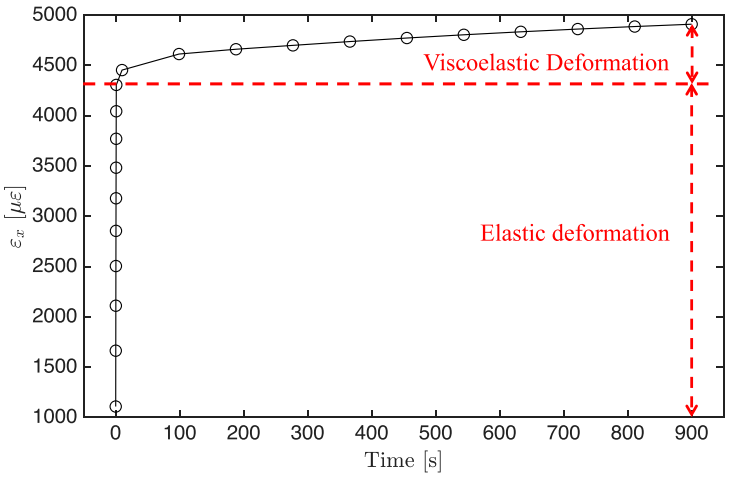

Figure 4. Time evolution of a selected example strain along x (ε_x). The response shows the rapid deformation occurring during the 1 s loading ramp, followed by a gradual increase in strain during the constant-load stage due to viscoelastic creep. The location where the example strain is measured can be observed in figure 6.

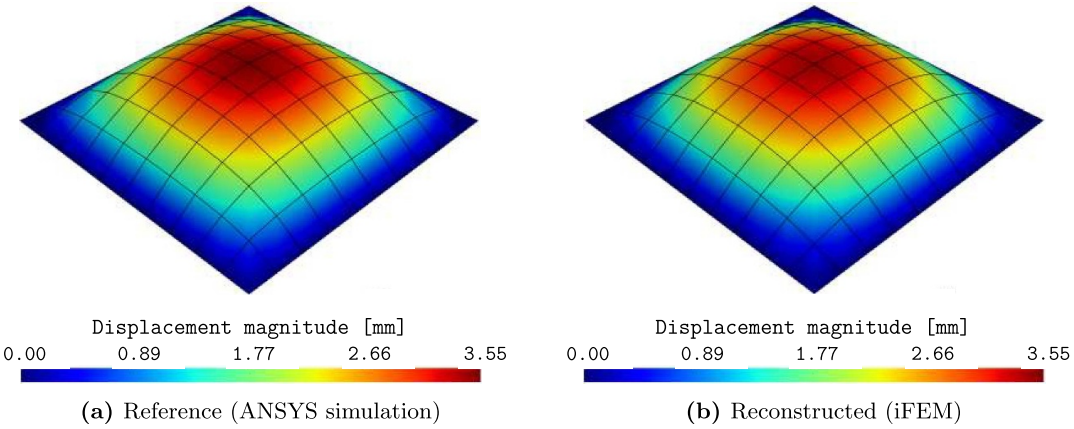

(a) Reference (ANSYS simulation) **(b)** Reconstructed (iFEM)

Figure 5. Displacement field of the abdominal patch. The contour plots are shown for (a) the results of the ANSYS simulation and (b) the reconstruction using iFEM of the model under the maximum intra-abdominal pressure of 0.0092 MPa and at the end of the monitored time, $t = 900$ section

configuration, fibre-optic strain sensors are considered. The optimal configuration has been obtained through an optimal sensor placement (OSP) procedure with the objective of minimising the displacement reconstruction error. The accuracy is assessed through the following percentage root mean squared error:

$$\%\mathrm{RMSE}_w = 100 \times \sqrt{\frac{1}{N}\sum_{i=1}^{N}\left(\frac{w_i - w_i^{\mathrm{ref}}}{w_{\mathrm{max}}^{\mathrm{ref}}}\right)^2} \tag{13}$$

where w_i are the reconstructed transverse displacements across the N nodes of the mesh, w_i^{ref} are the corresponding reference transverse displacements, computed from the analysis of the direct ANSYS mesh, and $w_{\mathrm{max}}^{\mathrm{ref}}$ is the maximum value of the reference transverse displacements. The minimisation is carried out using a Genetic Algorithm. For this application, the reference solution is obtained from the FE analysis of the patch without considering the viscoelastic regime. This condition is obtained by performing a linear static analysis of the patch under the load and boundary conditions already described, assuming a linear elastic material with the Young's modulus and Poisson's ratio defined in section 3.2.3. In accordance with the use of fibre optics, the optimiser is configured to select the best configuration of four lines of elements from the set of twenty lines connecting the centroids of the elements along the x and y directions of the patch. The final optimal configuration, which also helps to clarify the possible direction of the fibre lines, is shown in figure 6.

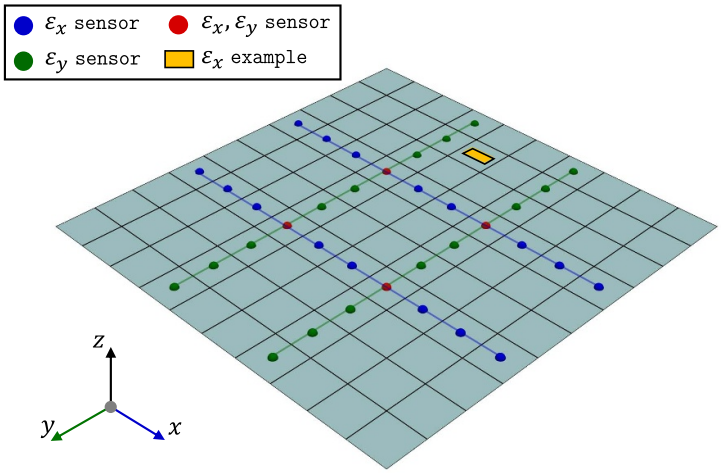

Figure 6. Sensor configuration. The configuration includes sensors measuring the strain along the x direction (ε_x sensors), the y direction (ε_y sensors), and locations where both components are measured (ε_x, ε_y sensors). The lines connecting the points represent a possible fibre optic installation layout to obtain the selected sensor locations. The figure also shows the location from which the strain time history in figure 4 is extracted (example ε_x sensor).

The initial linear-elastic solution was selected as the reference state for the OSP because the geometry, boundary conditions, material distribution and spatial pattern of the applied pressure remain unchanged throughout the analysis. Under these conditions, the creep-induced evolution observed in the present analysis is relatively limited and mainly consists of a gradual change in the magnitude of the strain and displacement fields, without substantial changes in their normalised spatial distributions. The sensor configuration obtained from the initial elastic reference state was subsequently kept unchanged and used for the iFEM reconstruction at every time step of the viscoelastic analysis.

The configuration includes two fibre optics running along the x and two along the y directions, which cross in four points, where the measurement in both directions is obtained. The high-density capabilities of fibre optics allow the measurement of strain at every centroid of the underlying elements, as shown in figure 6.

Once the iFEM model and the sensor configuration are set, the iFEM procedure is applied to the numerical data from the ANSYS simulation. Since the simulation is time-dependent, the displacement reconstruction with iFEM is performed separately for each time step. The procedure is very efficient and can be performed in real time. In fact, once the sensor configuration and the mesh are fixed, the coefficient matrix **K** in equation (8) remains constant over time and therefore needs to be inverted only once to compute the displacements. The vector **F**, on the other hand, must be continuously updated with new strain data from the sensors at each time step. Nevertheless, updating this vector and multiplying it by the already inverted matrix **K** is a computationally inexpensive process (equation (8)), thus enabling fast, real-time computation of the displacement field.

The time history of the reconstructed maximum transverse displacement, obtained through this procedure and located at the mid node of the patch, is shown in figure 7.

The plot shows that the iFEM reconstruction of the maximum transverse displacement is consistent with the reference displacement, especially in the phase where viscoelastic effects are dominant. A better evaluation of the iFEM performance can be obtained by analysing the trend of the percentage error in the reconstruction of the maximum displacement and the $\%\mathrm{RMSE}_w$, which assesses the overall accuracy of the reconstruction over the whole domain. The time histories of these two parameters are reported in figure 8.

The two error measures show a similar trend. The errors increase smoothly during the loading ramp (0–1 s), as shown in figure 9. Over this interval, the percentage error in the maximum transverse displacement rises from approximately 1.47% to 2.30%, while the $\%\mathrm{RMSE}_w$ rises from approximately 1.30% to 2.16%. During the subsequent constant-load viscoelastic phase, both errors increase only slightly, remaining consistently low and reaching approximately 2.46% and 2.26%, respectively.

These results show that the sensor configuration selected from the initial elastic reference state remains effective throughout the 900 s analysis. This demonstrates the temporal robustness of the selected layout for the present benchmark, although it does not prove that the same configuration remains mathematically optimal at every instant. If the normalised spatial strain distribution were to

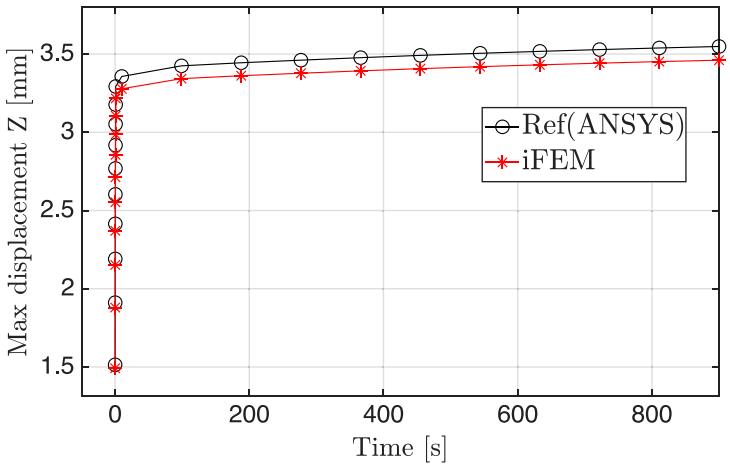

Figure 7. Time history of the mid-node transverse displacement. The plot shows the comparison between the reference maximum transverse displacement ($w_{\max}^{\text{ref}}$) and the reconstructed one ($w_{\max}$) obtained with iFEM.

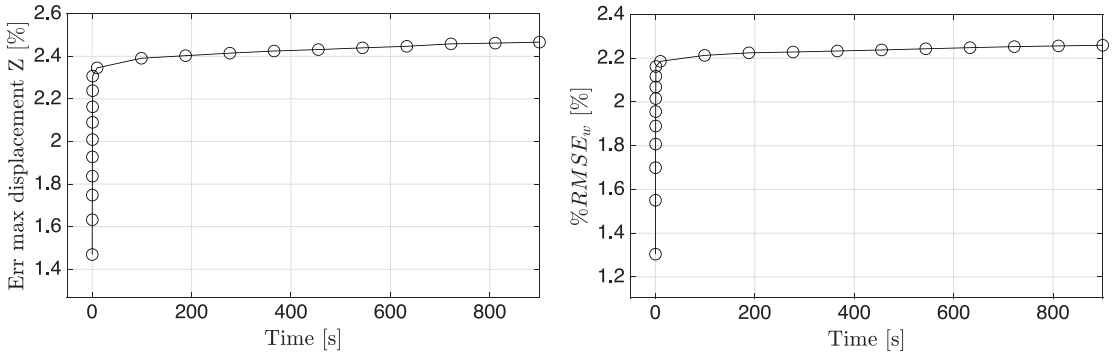

(a) Percentage Error on w_{max}^{ref} **(b)** $\%RMSE_w$

Figure 8. Time histories of the error in the iFEM reconstructions.

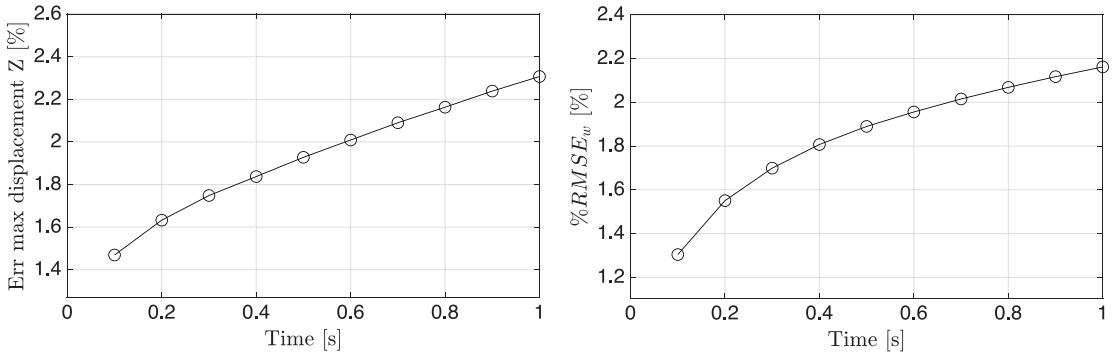

(a) Percentage Error on w_{max}^{ref} **(b)** $\%RMSE_w$

Figure 9. Time histories of the iFEM reconstruction errors during the loading phase (0–1 s).

change substantially because of non-proportional loading, spatially varying material properties, evolving boundary conditions or damage, the robustness of a layout optimised for a single reference state should be reassessed, for example using a multi-state OSP procedure. Finally, figure 5(b) presents the reconstructed displacement field at the last time step, where the effect of viscoelastic creep is maximum. The comparison with figure 5(a) highlights the accuracy of the displacement field reconstruction in the viscoelastic creep regime, demonstrating the capability of iFEM to effectively capture this behaviour.

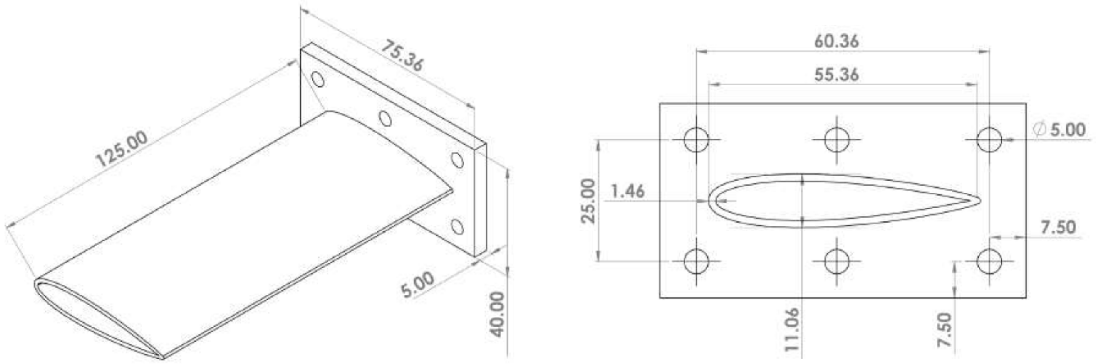

(a) Isometric view of the specimen (b) Front view of the specimen

Figure 10. Engineering drawings of the polymer beam specimen showing the beam profile attached to the flange which serves as the clamping system for the specimen; position and location of the clamping bolt holes are also shown (all dimensions indicated in the drawings are in mm).

3.3. Experimental case study: airfoil beam

3.3.1. Specimen and manufacturing

As additively manufactured polymeric components remain relatively unexplored within the field of shape sensing—where metallic and composite structures are more commonly investigated–a preliminary experimental study is conducted to assess their suitability for inverse analysis. In particular, the present case study aims to evaluate the performance of the iFEM when applied to a viscoelastic structure produced via additive manufacturing.

The beam specimen is designed as a scaled-down version of the thin-walled NACA 0016 airfoil beam investigated in [15]. The specimen has a total length of 125 mm, a chord length of 56 mm, and a uniform wall thickness of 1.46 mm. Detailed geometric dimensions are reported in figure 10.

Stereolithography (SLA) is selected as a simple, rapid, and cost-effective manufacturing technique for producing the prototype beam. In SLA, an ultraviolet laser selectively cures a photosensitive resin in a layer-by-layer process, resulting in components with high geometric accuracy and surface quality. Although the fabrication process is inherently layered, the resulting material behaviour is generally close to isotropic, with no marked differences between in-plane and inter-layer tensile properties. Nevertheless, all SLA resins are polymeric in nature and therefore exhibit viscoelastic behaviour, introducing additional material complexity that must be considered in the present investigation.

Specimens were fabricated using Tough 2000, a light-curable photopolymer resin with high stiffness and impact resistance [52]. In addition to the base material, the mechanical response of the printed component is influenced by printing parameters such as layer thickness, printing orientation, and post-curing conditions. For this reason, a preliminary material characterisation campaign is carried out to assess the mechanical properties of the printed resin and to inform the design of the beam experiment.

3.3.2. Material Testing

Dog-bone specimens were designed based on the geometry specified in ISO 527–2 and additively manufactured for preliminary mechanical characterisation of the printed resin as shown in figure 11(a). To maximise material quality, all specimens are printed using a layer thickness of 0.05 mm, corresponding to the minimum resolution available on the printer.

Two different printing orientations are investigated: one with the printing direction aligned with the longitudinal axis of the specimen, and one with the printing direction perpendicular to it. These configurations are selected to evaluate tensile behaviour both within a single layer and across multiple layers. Following fabrication, all specimens undergo a post-curing treatment at 60 °C for 30 min, after which they are allowed to cool naturally to room temperature. This procedure is known to increase tensile strength, albeit at the expense of ductility.

The tensile tests are performed at the *BIOMAST Lab*, (biomast.polito.it) using an MTS Insight testing machine with a displacement-controlled loading rate of 0.3 mm/s.

This characterisation campaign was conducted independently from that of Case 1 and was intended to provide representative stiffness and failure properties for the design of the airfoil-beam experiment, rather than to enable a direct comparison between the two polymeric materials.

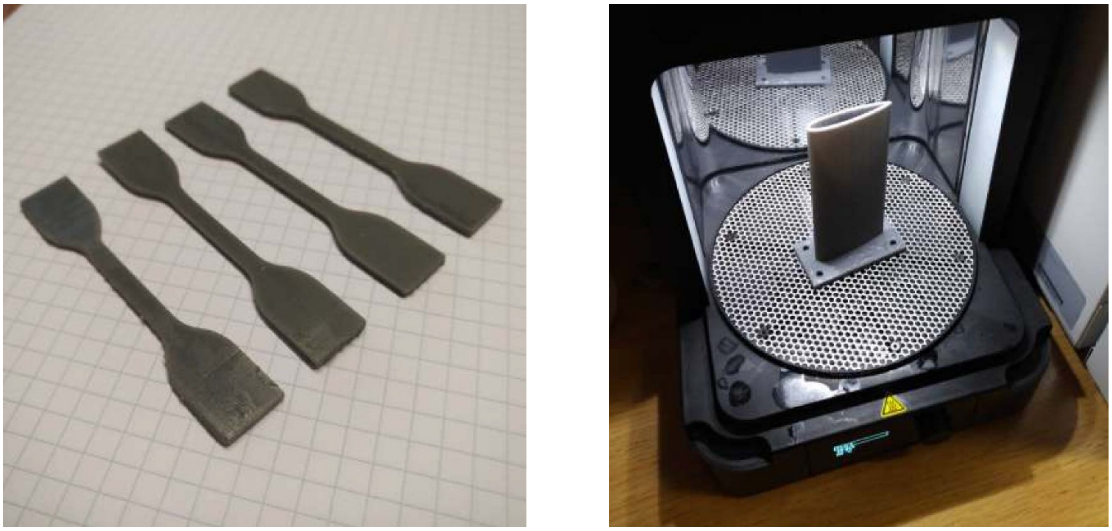

(a) (b)

Figure 11. Additively manufactured Tough 2000 resin parts printed using the Formlabs Form 2 printer: (a) specimens printed for tensile test campaign to characterise material behaviour, and (b) final printed and post-cured airfoil beam specimen.

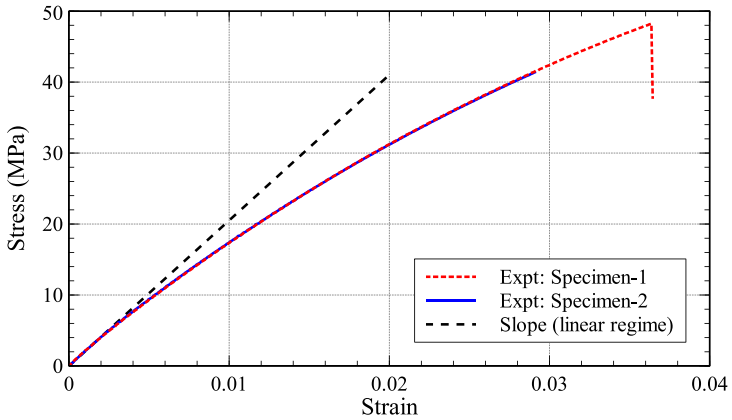

Figure 12. Results of the tensile test campaign. Stress–strain plots of the two polymer specimens: Specimen-1 refers to the test with the printing orientation corresponding to the longitudinal (and loaded) axis whereas Specimen-2 has the printing direction perpendicular to it. A line is also shown illustrating the slope of the linear regime of the curves.

Table 3. Results of the tensile test for the two specimens (θ_L represents the angle between the loading direction and plane of the layer).

Test specimen	θ_L	Stress at failure (MPa)	Strain at failure	Young's modulus (GPa)
1	0^0	48.2	0.036	2.0
2	90^0	41.3	0.029	2.05

Each specimen is loaded to failure, and the recorded force—displacement data are used to generate the stress–strain curves shown in figure 12.

The experimental results indicate no significant differences in stiffness between the two printing orientations, with only minor variations observed in the ultimate tensile strength. As expected for polymeric materials, the stress–strain curves exhibit a limited linear elastic regime (strain $\varepsilon < 0.05\%$), followed by a pronounced nonlinear response leading to failure. The average failure stress is approximately 44 MPa, while the Young's modulus, estimated from the initial linear portion of the curves, has an average value of 2.03 GPa (table 3).

These results are used to guide the design of the airfoil beam experiment, ensuring that maximum applied loads do not lead to failure. The final beam specimen is printed using the same resin, printing parameters, and post-curing procedure, with the printing direction aligned with the beam axis. The manufactured and post-cured beam is shown in figure 11(b).

The tensile tests were intended to estimate the initial stiffness of the printed material and to assess the influence of printing orientation. They did not constitute a time-dependent constitutive characterisation of the Tough 2000 resin. No dedicated creep-compliance or stress-relaxation tests were performed on the material used for the beam; therefore, the available experimental data do not permit the identification of time-dependent viscoelastic parameters or the calibration of a viscoelastic constitutive model. This does not affect the present iFEM validation, since the inverse reconstruction uses the experimentally measured strain histories directly and does not require a constitutive model of the beam material.

3.3.3. Experimental Setup and Testing

The final prototype features a thin-walled, symmetric NACA 0016 airfoil cross-section. Compared to the numerical cases in [15], the trailing edge is slightly rounded to facilitate manufacturing and handling.

The beam was tested as a cantilever with a concentrated transverse load applied at the tip. The test was conducted at the BIOMAST Lab (biomast.polito.it). Cantilever restraint was achieved through a flange printed integrally at the root and bolted to a rigid steel plate. Given the high stiffness of the steel support relative to the polymer beam, deformations of the plate were negligible, and the boundary condition was assumed fixed. A preliminary finite element model using the material properties in table 3 confirmed negligible axial displacement at the root, supporting this assumption, while also serving as practical validation of the clamping configuration.

The experimental set-up is shown in figure 13. The tip load was applied via a custom rib with three loading holes (using the central one, thus having the force aligned with the z-axis, figure 14). Vertical tip deflection was measured with an LVDT (HBK WI Displacement Transducer with 0.001 mm resolution and $\pm$ 1% sensitivity error) positioned near the tip and aligned with the same z-axis. For iFEM strain input, three strain-gauges were bonded near mid-span along the beam axis (see figures 14 and 15) and strains are measured with an acquisition frequency of 1 Hz. In particular, the three strain sensors share the same axial location ($x = 3L/5$ from the clamped end) and are all oriented along the beam axis to measure axial strain components. The position of the strain-gauges on the cross-section is shown in figure 14. Due to the limited beam length, a single *iEB2*, Bernoulli-Euler inverse beam element was employed, requiring axial and bending sectional strains at a minimum of two axial locations [16, 43]. Measured strains near mid-span, together with the assumption of vanishing strains at the free tip, were linearly interpolated along the beam to provide input for iFEM at two sections ($x = L/3$ and $x = 2L/3$). To quantify the error contribution due to the linear-strain assumption, an iFEM analysis is performed using strains obtained from a high-fidelity beam model developed in Abaqus. The beam is meshed using 347 102 C3D10 (quadratic tetrahedral) elements and is assumed to be made of a linear-elastic material with the following properties (based on the tensile test): $E = 2.03$ GPa and $\nu = 0.4$. For a concentrated tip load of 1 N, the FE analysis produced a beam tip displacement of 0.183 mm. iFEM analysis is performed using one iEB2 element and the displacement errors are reported for three different input strain scenarios: (a) 12.4% using strains measured at $L/3$ and $2L/3$, (b) 6.8% using strain measured at $3L/5$ and interpolated to $L/3$ and $2L/3$, and (c) 12.9% using case-(b) with 10% Gaussian noise. The results indicate no deterioration in accuracy due to the linear-strain assumption. The lower error obtained with the interpolated strain field should not be interpreted as evidence that interpolation generally improves iFEM accuracy. Rather, for the present configuration, it may reflect a case-specific compensation between the interpolation assumption and the modelling approximation associated with the use of a single iEB2 element, which does not account for all deformation components represented by the three-dimensional finite element model.

For the airfoil beam under a constant tip load of 0.7 N, the strain history (figure 16) exhibited a clear time-dependent response: an almost instantaneous elastic strain followed by gradual creep. Upon unloading, an immediate elastic recovery was observed, followed by slower viscoelastic recovery.

Strains remained below approximately 0.05%, indicating that the experiment was conducted within a small-strain regime. The observed time-dependent increase under sustained loading and delayed response after unloading are consistent with viscoelastic creep and recovery, although the available measurements do not permit the observed time-dependent response to be attributed to a specific viscoelastic behaviour.

This viscoelastic airfoil beam provides an ideal benchmark for assessing iFEM in the presence of time-dependent material behaviour. Moreover, the beam assumption is justified: for bending about the

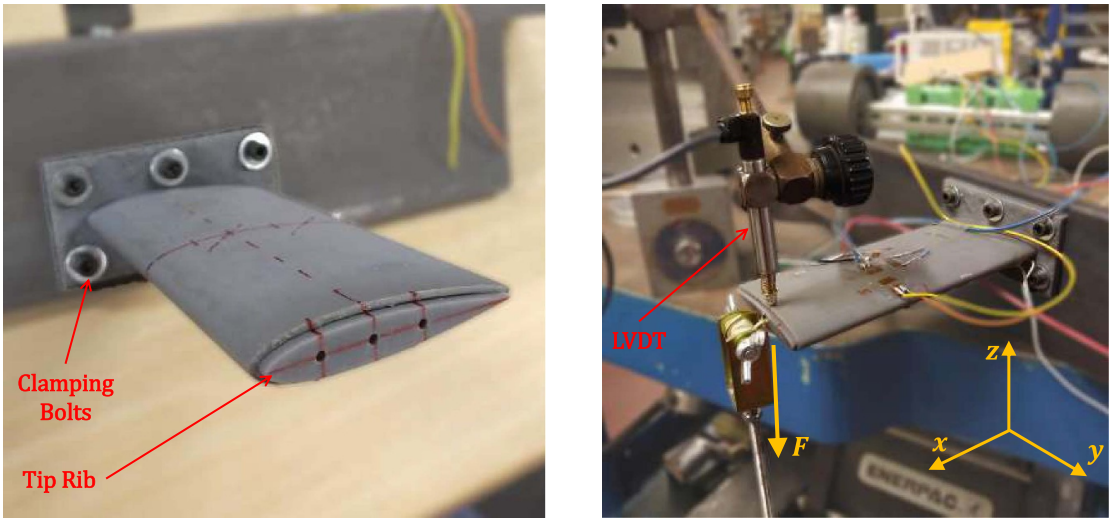

Figure 13. Images of the experimental setup: (a) beam specimen clamped onto a metallic base, (b) the instrumented sensors, loading setup and LVDT locations.

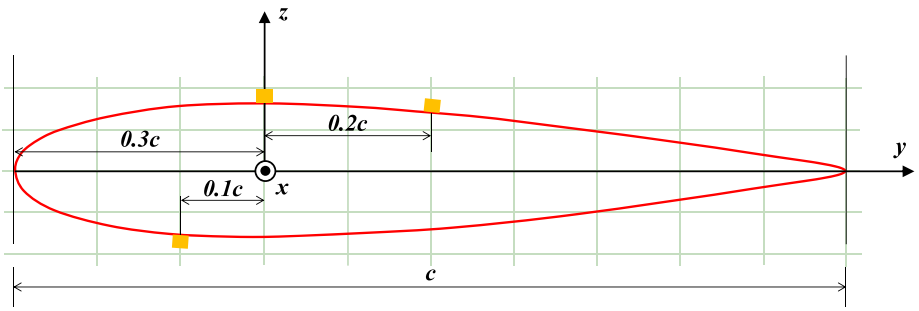

Figure 14. Airfoil beam cross-section, with reference axes and position of the axial strain-gauges.

y-axis, the length-to-height ratio is approximately 11.3. High-fidelity finite element simulations compared with shear-corrected analytical solutions showed a tip deflection difference of 2.5%, confirming the applicability of beam theory.

A maximum tip load of 4.3 N was applied in six increments, followed by complete unloading, allowing time for stabilisation at each step. Full time histories enabled assessment of iFEM performance during loading and unloading, capturing elastic, viscoelastic, and recovery phases.

Figure 17 compares experimental and iFEM-reconstructed tip deflections, showing excellent agreement across elastic and viscoelastic regimes, with slightly reduced accuracy during unloading. Percentage errors (figure 18) remained below 5% for most of the test, with peak errors of approximately 10% at the end of unloading. For a more reliable assessment of reconstruction error, three additional metrics are calculated: absolute error, error normalised by the maximum tip displacement, and root mean square (RMS) error. At the end of the unloading phase, an absolute displacement error of 0.037 mm and normalised displacement error of 3.56% is noted, while the RMS error for the loading and unloading phase is 1.69% and 5.98%, respectively. These results confirm the high accuracy of the iFEM reconstruction with lower errors observed during beam loading compared to unloading.

Overall, the results indicate that iFEM can accurately reconstruct time-dependent deformations of a viscoelastic, additively manufactured airfoil beam, confirming its material-independence and highlighting its potential for shape sensing and structural health monitoring of polymer-based structures.

3.3.4. Applicability and limitations

The iFEM formulations employed in this study are based on linear strain-displacement relations and are therefore restricted to small strains and small rotations. These requirements are satisfied in the numerical and experimental cases considered here. Applications involving large rotations, large deformations or

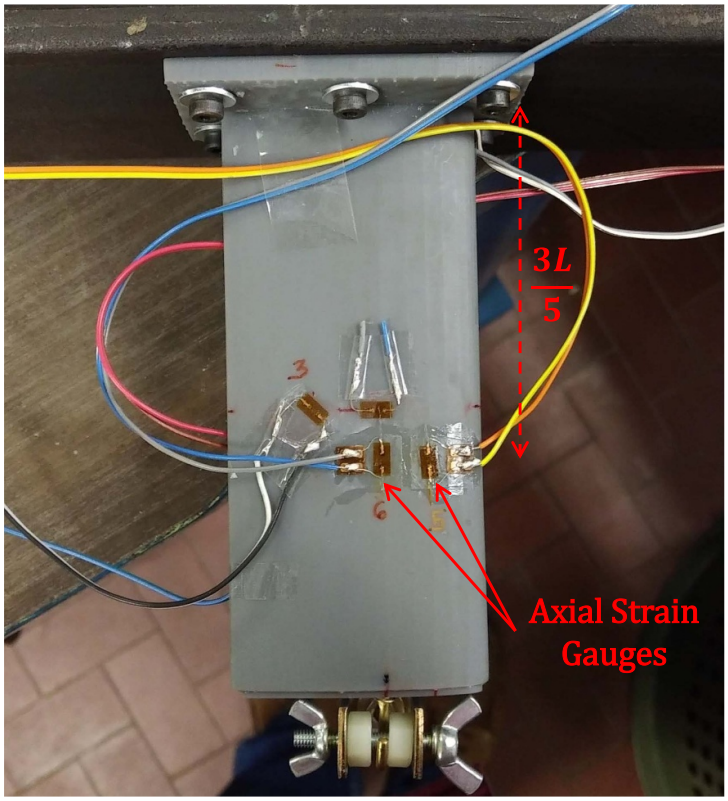

Figure 15. Top view of the beam specimen showing the location of the top axial strain gauges (see also figure 14). Other non-axial strain gauges shown in this figure were not used for the current iFEM application.

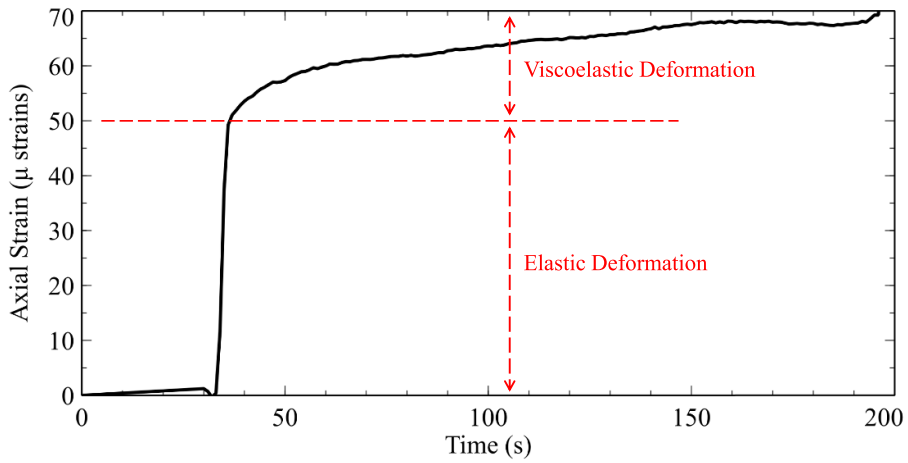

Figure 16. Variation of strain measurement over time for the polymer beam specimen loaded at the tip by a force of 0.7 N; the elastic and viscoelastic deformation regions are shown.

substantial changes in structural geometry would require a geometrically nonlinear inverse formulation with an updated kinematic description [53, 54].

The inverse reconstruction does not require the material to obey a linear viscoelastic constitutive law, because material parameters do not enter the iFEM equations. Material nonlinearity does not therefore invalidate iFEM solely because of its constitutive nature. However, if nonlinear viscoelasticity, yielding or damage produces large deformations, evolving geometry, strongly localised strain fields or discontinuities that are not adequately represented by the adopted inverse elements, the present formulation may no longer be appropriate.

Temperature variations may affect both the structural response and the strain measurements. Thermal strains contained in the sensor signals would also enter the reconstructed displacement field. Therefore, if the objective is to reconstruct purely mechanical deformation, thermal strains must be

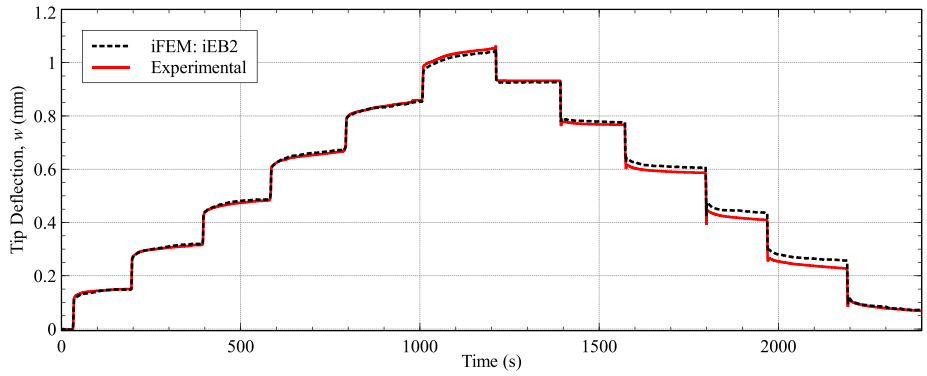

Figure 17. Results of the experimental test on the polymer beam specimen: comparison of tip deflection time history measured using a LVDT, and reconstructed using the iEB2 element.

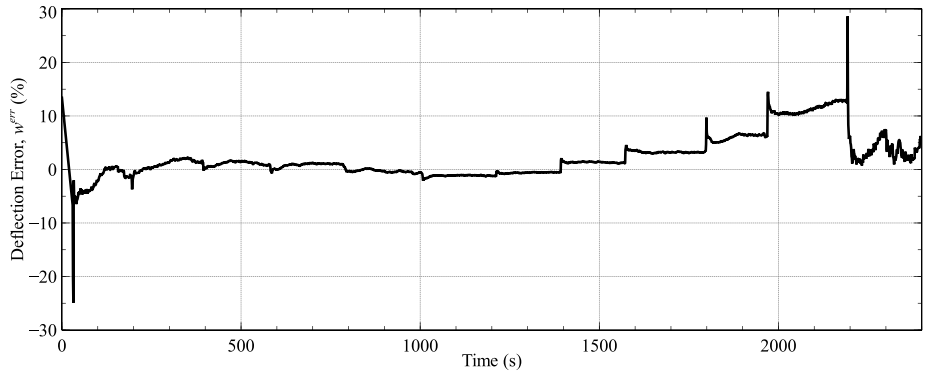

Figure 18. Results of the experimental test on the polymer beam specimen: time history of percentage error in tip deflection reconstructed using the iEB2 element.

independently measured or compensated. The present experiments were performed under approximately constant laboratory ambient-temperature conditions; temperature-dependent behaviour and time-temperature superposition were not investigated. It should also be emphasised that iFEM is material-independent, while the reconstruction remains dependent on the structural geometry and boundary conditions, the adopted kinematic assumptions, and the quality and spatial distribution of the strain measurements. Since measured strains constitute the direct input to the inverse problem, errors associated with sensor placement, calibration, measurement noise and strain interpolation may propagate into the reconstructed displacement field.

4. Conclusions

This work investigated the applicability of the iFEM for shape sensing in structures exhibiting time-dependent viscoelastic behaviour. Two complementary case studies were considered, including a numerical viscoelastic plate inspired by a biomedical abdominal patch and an experimental additively manufactured airfoil beam.

The results demonstrate that iFEM is capable of accurately reconstructing time-dependent deformation fields from sparse strain measurements, even in the presence of viscoelastic effects such as creep. In the numerical case study, high reconstruction accuracy was achieved, with error levels remaining low and stable over time despite the progressive evolution of deformation. The experimental investigation further confirmed the applicability of iFEM in realistic scenarios involving measurement noise, limited sensor configurations, and additively manufactured viscoelastic materials. The reconstructed displacement fields showed good agreement with experimental measurements across both loading and unloading phases, with slightly reduced accuracy during unloading, where the pointwise percentage error becomes more sensitive as the displacement approaches zero and experimental and reconstruction uncertainties may have a greater influence.

A key outcome of this study is that the iFEM formulation, being based solely on strain–displacement relations, does not require explicit knowledge of material constitutive behaviour. As a result, time-dependent effects contained in the measured strain histories are transferred to the reconstructed displacement fields, making the approach particularly suitable for viscoelastic systems and materials with uncertain or evolving properties.

Overall, the combined numerical and experimental validation highlights the potential of iFEM as a robust and computationally efficient tool for shape sensing and structural health monitoring of viscoelastic structures across a wide range of engineering applications, including biomedical devices, aerospace components, and additively manufactured systems.

Future work will focus on the extension of the methodology to more complex sensor configurations, the assessment of measurement noise effects, and the development of enhanced formulations to improve reconstruction accuracy under transient conditions and in the presence of measurement uncertainties.

Data availability statement

The data that support the findings of this study are available upon reasonable request from the authors. The data supporting this study are currently made available upon reasonable request because they were not originally organised and documented in a format suitable for deposition in a public repository. Providing the data upon request allows us to supply the relevant files together with the supporting information needed for their correct interpretation and potential reuse.

Funding

This research received no external funding.

Conflict of interest

The authors declare no conflict of interest.

ORCID iDs

Rinto Roy 0000-0003-4954-0166
Marco Esposito 0000-0001-6621-7542
Vito Burgio 0000-0002-4900-6257
Marco Gherlone 0000-0002-5711-0046
Cecilia Surace 0000-0002-3993-9432

References

[1] Gherlone M, Cerracchio P and Mattone M 2018 Shape sensing methods: Review and experimental comparison on wing-shaped plates *Prog. Aerosp. Sci.* **99** 14–26
[2] Roy R 2022 Developing Advanced Shape Sensing Methodologies for Aerospace Applications *Ph.D. dissertation* (Politecnico di Torino)
[3] Monsberger C M and Lienhart W 2021 Distributed fiber optic shape sensing of concrete structures *Sensors* **21** 6098
[4] Jiang Q, Li J and Masood D 2023 Fiber-optic-based force and shape sensing in surgical robots: a review *Sensor Rev.* **43** 52–71
[5] Galloway K C, Chen Y, Templeton E, Rife B, Godage I S and Barth E J 2019 Fiber optic shape sensing for soft robotics *Soft Robot.* **6** 671–84
[6] Chen Q, Zhang Y, Dong X, Cui J, Lu Y, Zheng P and Liu W 2026 A high-accuracy shape sensing method for deformation digital twin monitoring of thin-walled aircraft structures *Aerosp. Sci. Technol.* **168** 110960
[7] Zhang Q, Wen F, Wu X, Yang H, Li X, Luo P, Liu H, Wang Z, Herth F J F and Zhang X 2025 Shape sensing robotic assisted bronchoscopy versus virtual bronchoscopic navigation in the diagnosis of peripheral pulmonary nodules *Sci. Rep.* **15** 23950
[8] Shen W, He J, Yang G, Kong X, Bai H and Fang Z 2024 Shape sensing and kinematic control of a cable-driven continuum robot based on stretchable capacitive sensors *Sensors* **24** 3385
[9] Ko W L, Richards W L and Tran V T 2007 Displacement theories for in-flight deformed shape predictions of aerospace structures NASA/TP-2007-214612
[10] Bogert P B, Haugse E, Works B P, Gehrki R E and Martin L 2003 Structural shape identification from experimental strains using a modal transformation technique *Proc. 44th AIAA Structures Conf.* (https://doi.org/10.2514/6.2003-1626)
[11] Bruno R, Toomarian N and Salama M 1994 Shape estimation from incomplete measurements: a neural-net approach *Smart Mater. Struct.* **3** 92–97

[12] Khalid I, Qureshi Z A, Oterkus S and Oterkus E 2025 Progress in inverse finite element method for aerospace structural health monitoring applications *Prog. Aerosp. Sci.* **157** 101132
[13] Tessler A and Spangler J L 2005 A least-squares variational method for full-field reconstruction of elastic deformations in shear-deformable plates and shells *Comput. Methods Appl. Mech. Eng.* **194** 327–39
[14] Gherlone M, Cerracchio P, Mattone M, Di Sciuva M and Tessler A 2014 An inverse finite element method for beam shape sensing: theoretical framework and experimental validation *Smart Mater. Struct.* **23** 045027
[15] Roy R, Gherlone M and Surace C 2021 A shape sensing methodology for beams with generic cross-sections: application to airfoil beams *Aerosp. Sci. Technol.* **110** 106484
[16] Roy R, Surace C and Gherlone M 2024 Full-field deformation reconstruction of beams using the inverse finite element method: application to thin-walled structures *Thin-Walled Struct.* **200** 111907
[17] Esposito M, Roy R, Surace C and Gherlone M 2023 Hybrid shell-beam inverse finite element method for the shape sensing of stiffened thin-walled structures: formulation and experimental validation on a composite wing-shaped panel *Sensors* **23** 5962
[18] Esposito M and Gherlone M 2020 Composite wing box deformed-shape reconstruction based on measured strains: optimization and comparison of existing approaches *Aerosp. Sci. Technol.* **99** 105758
[19] Cerracchio P, Gherlone M, Di Sciuva M and Tessler A 2015 A novel approach for displacement and stress monitoring of sandwich structures based on the inverse finite element method *Compos. Struct.* **127** 69–76
[20] Savino P, Gherlone M, Tondolo F and Greco R 2021 Shape-sensing of beam elements undergoing material nonlinearities *Sensors* **21** 528
[21] Roy R, Tessler A, Surace C and Gherlone M 2022 Efficient shape sensing of plate structures using the inverse finite element method aided by strain pre-extrapolations *Thin-Walled Struct.* **180** 109798
[22] Oboe D, Sbarufatti C and Giglio M 2022 Physics-based strain pre-extrapolation technique for inverse finite element method *Mech. Syst. Signal Process.* **177** 109167
[23] Zhao Y, Du J, Bao H and Xu Q 2018 Optimal sensor placement based on eigenvalues analysis for sensing deformation of wing frame using iFEM *Sensors* **18** 2424
[24] Roy R, Tessler A, Surace C and Gherlone M 2020 Shape sensing of plate structures using the inverse finite element method: investigation of efficient strain–sensor patterns *Sensors* **20** 7049
[25] Wu M and Tan S 2024 Inverse finite element method with energy-based regularization for deformation reconstruction and structural health monitoring *Thin-Walled Struct.* **199** 111859
[26] Roy R, Gherlone M, Surace C and Tessler A 2021 Full-field strain reconstruction using uniaxial strain measurements: application to damage detection *Appl. Sci.* **11** 1681
[27] Kefal A, Tabrizi I and Yildiz M 2021 *Real-Time Monitoring of Crack Propagation in Fiber-Reinforced Composite Plates Using Ifem Methodology* (CRC Press) pp 345–53
[28] Oboe D, Poloni D, Sbarufatti C and Giglio M 2023 Towards automatic crack size estimation with ifem for structural health monitoring *Sensors* **23** 3406
[29] Bardiani J, Ragani R F, Pinello L, Kefal A, Manes A and Sbarufatti C 2026 Shape sensing and damage detection of composite pressure vessels using inverse finite element method coupled with physics-based strain pre-extrapolation *Thin-Walled Struct.* **218** 113935
[30] Biscotti V, Roy R and Gherlone M 2025 Shape monitoring of morphing wing structures using the inverse finite element method *Comput. Struct.* **309** 107652
[31] Chua C K and Leong K F 2017 *3D Printing and Additive Manufacturing Principles and Applications 5th edn of Rapid Prototyping* (World Scientific)
[32] Afridi A, Rashid A A and Koç M 2024 Recent advances in the development of stereolithography-based additive manufacturing processes: a review of applications and challenges *Bioprinting* **43** e00360
[33] Vivegananthan P, Gao S, Ji W, Fan H, Han C and Zhou K 2024 Recent progress on 3D printing of lightweight metal thin-walled structures *Adv. Mater.* **36** 2402130
[34] Zhu G, von Coelln N, Hou Y, Vazquez-Martel C, Spiegel C A, Tegeder P and Blasco E 2024 Digital light 3D printing of double thermoplastics with customizable mechanical properties and versatile reprocessability *Adv. Mater.* **36** e2401561
[35] Sekmen K, Rehbein T, Johlitz M, Lion A and Constantinescu A 2023 Curing-dependent thermo-viscoelastic and shrinkage behaviour of photopolymers *Mech. Mater.* **179** 104566
[36] Gibson I, Rosen D W and Stucker B 2021 *Additive Manufacturing Technologies: 3D Printing, Rapid Prototyping and Direct Digital Manufacturing* (Springer) (https://doi.org/10.1007/978-1-4939-2113-3)
[37] Gobi R, Ravichandiran P, Babu R S and Yoo D J 2021 Biopolymer and synthetic polymer-based nanocomposites in wound dressing applications: a review *Polymers* **13** 1962
[38] Li P, Yan Z, Zhang L, Liu Y, Leng J and Lau K T 2014 Monitoring of deployment process of shape memory polymers for morphing structures with embedded fibre Bragg grating sensors *J. Intell. Mater. Syst. Struct.* **25** 1224–32
[39] Lun T L T, Wang K, Ho J D L, Lee K H, Sze K Y and Kwok K W 2019 Real-time surface shape sensing for soft and flexible structures using fiber bragg gratings *IEEE Robot. Autom. Lett.* **4** 1454–61
[40] Feliu-Talegon D, Adamu Y A, Mathew A T, Alkayas A Y and Renda F 2025 Advancing soft robot proprioception through 6d strain sensors embedding *Soft Robot.* **12** 465–76
[41] Gherlone M, Cerracchio P, Mattone M, Di Sciuva M and Tessler A 2012 Shape sensing of 3D frame structures using an inverse finite element method *Int. J. Solids Struct.* **49** 3100–12
[42] Esposito M, Roy R, Surace C and Gherlone M 2023 Structural deformation reconstruction using the hybrid shell-beam inverse finite element method: experimental application on a thin-walled stiffened panel *Compdyn* 3404–14
[43] Savino P, Gherlone M and Tondolo F 2019 Shape sensing with inverse finite element method for slender structures *Struct. Eng. Mech.* **72** 217–27
[44] Evonik Nutrition & Care GmbH 2015 *RESOMER® Product Range (Version 2.6)* (Evonik)
[45] Burgio V, Di Giacinti M, Reinoso M R, Tuveri V, Antonaci P and Surace C 2026 Surace *Mechanical characterization and constitutive modelling of commercial biopolymers and their blends for biomedical applications J. Mech. Behav. Biomed. Mater.* **173** 107205
[46] Reinoso M R *et al* 2021 Effects of the manufacturing methods on the mechanical properties of a medical-grade copolymer poly(L-lactide-co-D,L-lactide) and Poly(L-lactide-co-ε-caprolactone) Blend *Materials* **14** 6381
[47] Eng C C, Ibrahim N A, Zainuddin N, Ariffin H, Yunus W M Z W, Then Y Y and Teh C C 2013 Enhancement of mechanical and thermal properties of polylactic acid/polycaprolactone blends by hydrophilic nanoclay *Indian J. Mater. Sci.* **2013** 816503

[48] García-Campo M J, Boronat T, Quiles-Carrillo L, Balart R and Montanes N 2018 Manufacturing and characterization of toughened poly(lactic acid) (PLA) formulations by ternary blends with biopolyesters *Polymers* **10** 3
[49] Reinoso M R, Burgio V, Tuttobene C, Tuveri V, Antonaci P and Surace C 2026 Mechanical characterization of P(L/DL)LA–PLCL co-polymeric blend for biomedical applications *J. Phys.: Conf. Ser.* **3253** 012012
[50] Cobb W S, Burns J M, Kercher K W, Matthews B D, James Norton H and Todd Heniford B 2005 Normal intraabdominal pressure in healthy adults *J Surg Res.* **129** 231–5
[51] Esposito M, Mattone M and Gherlone M 2022 Experimental shape sensing and load identification on a stiffened panel: a comparative study *Sensors* **22** 1064
[52] Riccio C, Civera M, Ruiz O G, Pedullà P, Reinoso M R, Tommasi G, Vollaro M, Burgio V and Surace C 2021 Effects of curing on photosensitive resins in SLA additive manufacturing *Appl. Mech.* **2** 942–55
[53] Tessler A, Roy R, Esposito M, Surace C and Gherlone M 2018 Shape sensing of plate and shell structures undergoing large displacements using the inverse finite element method *Shock Vib.* **1** 8076085
[54] Belur M Y and Kefal A 2026 Geometrically nonlinear deformation reconstruction of membrane structures using inverse finite element method *AIP Conf. Proc.* **3489** 280071